A data-driven modelling and optimization framework for variable-thickness integrally stiffened shells

Hongqing Li [a], Zengcong Li [a], Zhizhong Cheng [b], Zhiyong Zhou [b], Gang Wang [b], Bo Wang [a], Kuo Tian [a,c,*]

[a] *Department of Engineering Mechanics, State Key Laboratory of Structural Analysis for Industrial Equipment, Dalian University of Technology, Dalian, 116024, China*
[b] *Institute of Spacecraft System Engineering, China Academy of Space Technology, Beijing, 100094, China*
[c] *DUT Artificial Intelligence Institute, Dalian, 116024, China*

A B S T R A C T

The integrally stiffened shells possess the advantages of high specific strength, high specific rigidity and excellent sealing performance, which have been widely used in the load-carrying structure of next-generation manned spacecraft and cargo spacecraft. However, the automatic modelling and optimization of the variable-thickness (VT) integrally stiffened shell are challenging due to the diverse stiffener configurations and the VT skin at multiple corners. To address this issue, a novel data-driven modelling and optimization framework is proposed for the VT integrally stiffened shell in this paper. Firstly, a novel mesh deformation method is proposed for modelling the VT integrally stiffened shell combining the radial basis function (RBF) surrogate model and nonuniform rational B-splines (NURBS). By means of the RBF surrogate model, the mapping relationship between the background mesh domain of curved shell and the target mesh domain of flat plate is trained, and then the equal-thickness (ET) stiffened flat plate is transformed into the VT stiffened flat plate by moving coordinates of nodes. In order to realize the accurate description of the VT stiffened flat plate, NURBS method is used to describe the coordinates of nodes. Finally, the VT stiffened flat plate is transformed into the VT integrally stiffened shell by the mapping relationship. In order to verify the accuracy of the proposed method, a skin-stiffener verticality detection method is proposed for stiffened curved shells. Moreover, based on the deep neural network (DNN) method, a data-driven stiffener layout optimization method is established to minimize the structural weight of the VT integrally stiffened shell. To illustrate the effectiveness of the proposed method, an example of the integrally stiffened shell under internal pressure is carried out. The average value of the detection results of skin-stiffener verticality for the integrally stiffened shell under internal pressure is less than 0.29°, indicating the high accuracy of the proposed modelling method. Compared with the initial result and the optimal result of the equal-thickness integrally stiffened shell, the optimal result of the VT integrally stiffened shell achieves a structural weight reduction of 14.77% and 10.31%, respectively. Optimization results indicate the effectiveness of the proposed optimization framework and the advantage of VT integrally stiffened shells in lightweight design.

© 2022 Elsevier Masson SAS. All rights reserved.

1. Introduction

Thin-walled structures are widely used in modern aircraft, launch vehicles, spacecraft, and marine structures [1–5]. Among them, the integrally stiffened shell is representative and competitive, which has high specific stiffness and specific strength, and demonstrate excellent performance when enables to improve the seal performance and fatigue resistance of the structure. Although the integrally stiffened shell has been widely used in launch vehicle and manned spacecraft cabins, there exist great differences in the structure due to different requirements for their uses, environments and reliability. In order to make full use of space and make the structure lighter, the stiffeners of manned spacecraft are mostly distributed on the outer surface of the skin, such as the propulsion module of the US space shuttle and the various types of

(a) NASA Orion pressure vessel   (b) typical FE model   (c) 1/4 FE model
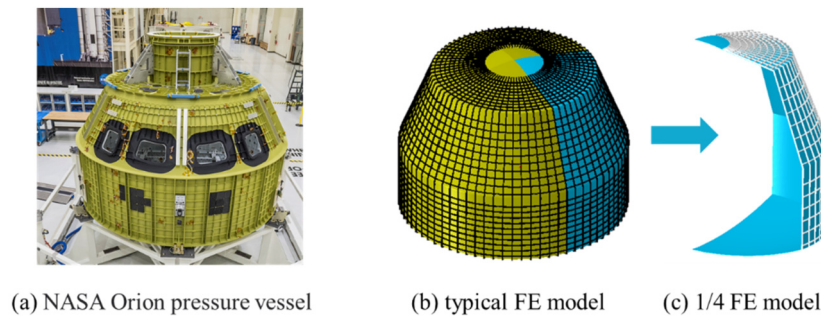
Fig. 1. Schematic diagrams of the integrally stiffened shell. (a) NASA Orion pressure vessel (from https://www.flickr.com/photos/nasaorion/); (b) typical FE model; (c) 1/4 FE model.

the international space station experimental cabin [6,7]. For example, the Orion pressure vessel is the bottom structure of the crew compartment of NASA's Orion spacecraft, as shown in Fig. 1(a). Since the main load for the integrally stiffened shells is internal pressure and the curvature of the structure changes abruptly at the corner of the structure, which leads to stress concentration at multiple corners. Therefore, the VT integrally stiffened shells have a more obvious advantage in lightweight design.

The technology of integrally stiffened shells modelling on cylindrical shells used in launch vehicles has experienced booming development and various stiffener configurations have been developed, such as orthogonal stiffeners [8,9], triangular stiffeners [10,11], oblique orthogonal stiffeners [12,13], Kagome stiffeners [16], and hierarchical stiffened shells [14,15]. The corresponding parametric finite element (FE) modelling methods and equivalent modelling methods have been widely investigated [17,18]. In order to improve the linear buckling analysis and optimization efficiency of the stiffened cylindrical shell structure. Chen et al. [19] developed an integrated equivalent stiffness method to describe a grid structure with or without laminate skins, which could be incorporated with exact FE modelling to obtain a refined stress analysis. Tian et al. [20] employed a fast numerical solution of asymptotic homogenization method for the equivalence of stiffened shells, achieving high prediction accuracy and efficiency. Tian et al. [21] established numerical-based smeared stiffener method (NSSM), which can quickly predict the linear buckling load and buckling mode of hierarchical stiffened shells. Jiang et al. [22] established the theoretical models to reveal the failure modes and predict the ultimate load of the compressed orthogonal stiffened cylinder by using the smearing method. In order to meet the needs of space missions on the manned spacecraft cabin, the VT integrally stiffened shells are used as its main structure. Under the condition of satisfying the requirements of load-bearing stability, internal pressure strength, overall air tightness, and equipment connection, it is challenging to design VT integrally stiffened shells efficiently.

The structural characteristics of the VT integrally stiffened shell are generally characterized by VT skins and the non-straight generatrix, which makes the rapid modelling and analysis methods of straight cylindrical shells unable to be directly applied. The current mainstream design method is to firstly optimize the shape based on a two-dimensional axisymmetric model and then optimize the design of the stiffeners after fixing the cross-sectional shape. The shape optimization of axisymmetric pressure vessels has been extensively investigated [23–25], which can be obtained by numeral calculations or FE optimization. But due to the complexity of the optimized cross-sectional shape, it is a problem to optimize the layout of the three-dimensional stiffeners on the model. Traditional modelling method mainly generates surface stiffened structures through the mapping of coordinate system [26]. In recent

years, NURBS method [27] and mesh deformation method [28–30] have been widely used in the rapid modelling complex structures because of their high efficiency, controllability and easy automation. Feng et al. [31] developed an effective B-spline parameterization method for stiffener layout optimization of shell structures. Porziani et al. [32] proposed a mesh morphing approach based on radial basis functions that is suitable for complex industrial applications. Many efforts have been made to further improve the data-reduction RBF method by modifying control points [33,34]. Tian et al. [35] proposed a novel mesh deformation method for automatic modelling of undevelopable stiffened curved shells by mesh deformation method. The above modelling methods are oriented to the design of curvilinear stiffeners or the two-dimensional section design with variable thickness. There are very rare studies focusing on the VT integrally stiffened shell according to the investigation. Therefore, a main research objective of this paper is to establish an intelligent model reconstruction method for the VT integrally stiffened shell based on data-driven mesh deformation and mapping.

To build a VT integrally stiffened shell, a common way is to shape the curve by several control points and describe the layout and path of stiffeners by several parameters. Then, optimization procedure is performed to find optimal results for these parameters. Many effective and efficient optimization strategies have been developed by researchers in the past few years. Surrogate model is the most popular solution, which including Radial Basis Function (RBF), Response Surface Method (RSM) and Kriging, etc. Wang et al. [36] established a multilevel optimization method to search the global optimal solution. Keshtegar et al. [37] proposed a bi-loop optimization framework by combining response surface method and Gaussian global-best harmony search, which was aimed to search the optimum solution of stiffened shells. Tian et al. [38] developed an enhanced variance reduction method for stiffened shells by combining the Latinized partially stratified sampling with multi-fidelity methods. Due to the advancement of computer technology, machine learning methods have been widely used to solve complex problems in many fields, such as aerodynamic shape optimization [39], fuel-optimal problem [40], autonomous navigation [41], trajectory optimization [42] and aerospace design [43,44]. Recently, machine learning methods replace the traditional analysis methods to improve the computational efficiency of complex optimization [45]. An enhanced variable-fidelity surrogate-based optimization framework based on the Gaussian Process regression and fuzzy clustering method was established, which achieved higher prediction accuracy than the traditional variable-fidelity surrogate models [46]. A novel establishment method of the variable-fidelity surrogate model driven by transfer learning has been proposed for shell buckling prediction problems such as buckling prediction of variable-stiffness composite shells [47]. In particular, the DNN

method has been shown better performance than classical machine learning methods in solving real-world problems [48–50].

According to above literature investigation, there is a lack of efficient automatic modelling and optimization methods for the VT integrally stiffened shell, which is regarded as the research objective of this paper. This paper is arranged as follows. Firstly, a novel mesh deformation method is developed for automatic modelling of the VT integrally stiffened shell based on RBF surrogate model method and NURBS method in Section 2.1. Based on the DNN method, the data-driven optimization framework is established for the VT integrally stiffened shell in Section 2.2. Then, a representative example comparing the VT integrally stiffened shell and the ET integrally stiffened shell is carried out to verify the effectiveness of the proposed framework in Section 3. The conclusion is drawn in Section 4.

2. Data-driven modelling and optimization framework for the VT integrally stiffened shell

2.1. Mesh deformation method for modelling the VT integrally stiffened shell

For the engineering modelling of the VT integrally stiffened shell, the traditional method is usually to perform manual modelling in CAD modelling software [51] such as Pro/Engineer and Unigraphics (UG). When the details of the VT integrally stiffened shell are complicated, the model reconstruction steps are tedious, time-consuming and low-accuracy. By the way, when the CAD model is imported into CAE software, it is easy to cause problems such as mesh division failure and mesh element deformity.

In order to solve this problem, this section proposes a modelling method for the VT integrally stiffened shell based on mesh deformation technology. Its basic idea is to firstly build the stiffened flat plate, and then train the mapping relationship between the flat plate (referred to as the background mesh domain) and the integrally stiffened shell (referred to as the target mesh domain). Then ET stiffened flat plate is transformed into the VT stiffened flat plate by using NURBS method to describe the coordinates of nodes, and finally the VT stiffened flat plate is transformed into the VT integrally stiffened shell by means of the mapping relationship. Especially in order to obtain VT FE model, the skin is established by solid elements. When the skin thickness changes by moving nodes of elements, the corresponding area of the stiffener height is automatically adjusted.

In this paper, RBF surrogate model [52] is used to train the mapping relationship between the flat plate (referred to as the background mesh domain) and the integrally stiffened shell (referred to as the target mesh domain). The RBF surrogate model is widely used in the field of data fitting since the model can fit nonlinear functions and has excellent generalization ability [53,54]. In recent years, Jin [55] conclude that RBF is the most dependable method in most situations in terms of accuracy and robustness. For the RBF interpolation method, its general form is:

$$g(r) = \sum_{i=1}^{N_c} \alpha_i \phi(||r - r_i||) \tag{1}$$

where r is an n-dimensional vector of variables, r_i is the vector of design variables at the ith sampling point, $||r-r_i||$ is the Euclidean distance, N_c is the total number of selected data points, ϕ is a radial function and α_i is the unknown coefficient of the ith RBF node.

The most popular radial functions are listed below [56]:

$$\phi(\eta) = \begin{cases} e^{\left(\frac{-\eta^2}{c^2}\right)} & \text{(Gauss)} \\ (\eta^2 + c^2)^{\frac{1}{2}} & \text{(Multiquadric)} \\ (\eta^2 + c^2)^{-\frac{1}{2}} & \text{(Inversemultiquadric)} \end{cases} \tag{2}$$

In this section, the Wendland C2 function is selected as the radial function, and the expression is:

$$\phi(\eta) = (1 - \eta)^4 (1 + 4\eta) \tag{3}$$

where $\eta = ||r_i - r||/d$, d is the radius of action of the RBF. When $\eta > 1$, $\phi(\eta)$ is equal to zero.

In order to realize the accurate description of the VT stiffened flat plate, this paper uses the NURBS curve to describe the thickness distribution. Compared with the traditional curve design, NURBS [57–59] is the best representative form for curve and surface. Since the forming curve is smooth and the curvature can be kept continuous after local modification, NURBS curve can fit a variety of complex shapes.

The proposed method mainly includes the following steps.

Step 1: The background mesh domain and the target mesh domain should be defined firstly. The target mesh domain is the FE solid model containing the design domain of the VT integrally stiffened shell. A FE solid model of simple plane is suggested to be chosen as the background mesh domain, which has similar topological characteristics with the target mesh domain and identical number of nodes. The flat plate is selected as the background mesh domain here, and schematic diagrams of the background mesh domain and the target mesh domain are displayed in Fig. 2. In order to ensure the accuracy of mesh deformation, the interpolation method rather than extrapolation method is adopted. The height of two FE solid models is required to be greater than the sum of the largest skin thickness and the largest stiffeners height. The height of the background mesh domain and the height of the target mesh domain should be the same, so that the height of the stiffeners on the flat plate is identical with the height of the stiffeners after deformation, which is convenient for modelling description.

Step 2: The RBF surrogate model is employed to train the mapping relationship between these two control point sets of the background mesh domain and the target mesh domain. The input of the training model is the coordinates of all control points of the background mesh domain in Step 1. Since each control point includes coordinate values along 3 directions, its vector form can be expressed as $X = (X_1, X_2, \ldots, X_N)$, where $X_i = (x_{i1}, x_{i2}, x_{i3})^T$ $(1 \le i \le N)$, and N is the number of the control points. The output of the training model is the coordinates of all control points of the target mesh domain in Step 1. It can be expressed as $Y = (Y_1, Y_2, \ldots, Y_N)$, where $Y_i = (y_{i1}, y_{i2}, y_{i3})^T$ $(1 \le i \le N)$.

Step 3: The VT stiffened flat plate is obtained by moving coordinates of nodes. Firstly, the ET stiffened flat plate is established, which contains solid FE model for skin and shell FE model for stiffeners. Several NURBS control points are distributed on the areas of stiffened flat plate at multiple corners. For the stiffened flat plate model, the thickness distribution of the multiple corners can be changed by modifying the shape of a section. Therefore, this paper uses a two-dimensional NURBS curve generated by the NURBS control points to fit the VT area. By changing the coordinates of the control points, the coordinates of the grid nodes in the multiple corners can be adjusted according to the generated NURBS curve. The coordinate values of control points are evenly distributed along the length direction μ, and their spacing depends on the length d of the area requiring variable thickness and the number of control points N_{cp}. The coordinate value of the control point along the thickness direction v is determined by the given design parameter
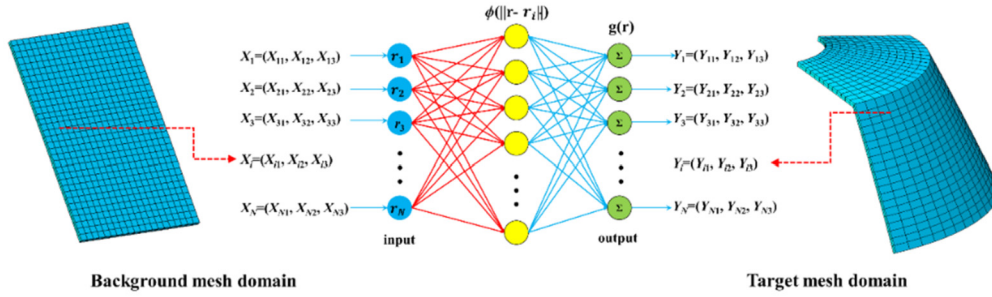
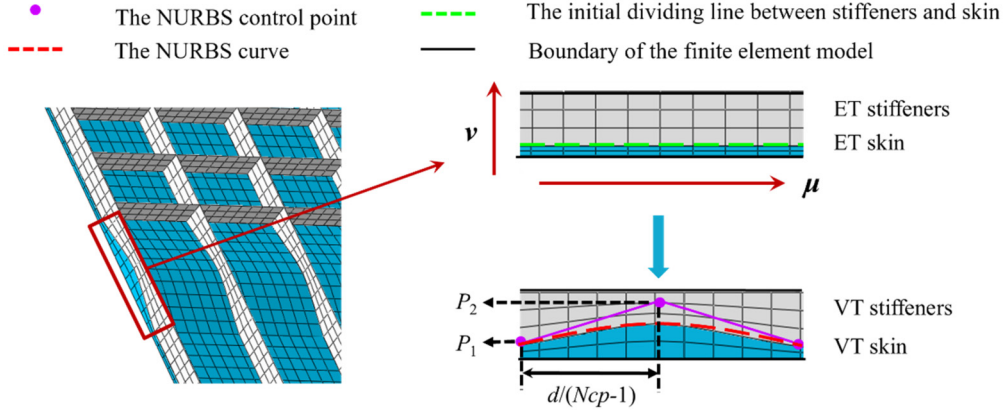**Fig. 2.** Schematic diagrams of building RBF surrogate model.

Fig. 3. Schematic diagrams of building VT stiffened flat plate. (For interpretation of the colours in the figure(s), the reader is referred to the web version of this article.)

P_i, as shown in Fig. 3. Since the control points are uniform distributed on the corner area evenly, the thickness distribution of the corner area is further reduced to one-dimensional problem, which can be changed by modifying the coordinates of the control points along the thickness direction. Since the two stiffened shells are connected by a corner, the thickness changes are transitioned at the corner. In other words, the thickness of the previous stiffened shell determines the coordinates of the initial control point at the corner, and the coordinates of the last control point in the corner determines the thickness of the next stiffened shell. In this way, the thickness variation of the entire flat plate, including the thickness of the corner area and the thickness of each stiffened shell, can be described by the height of several control points. Since the sum of the stiffener height and the skin thickness is fixed, when the thickness is changed due to the adjustment of the NURBS control points, the height for stiffeners will automatically change to keep the sum fixedly. The schematic diagrams of VT stiffened flat plate are displayed in Fig. 3.

Step 4: Based on the mapping relationship in Step 2, the VT stiffened flat plate established in Step 3 can be transformed into the integrally stiffened shell, which is displayed in Fig. 4. In other word, FE models of the VT stiffened flat plate and the VT integrally stiffened shell are the input and the output of the RBF surrogate model. In order to illustrate the robustness of the method, integrally stiffened shells with different stiffener configurations are established in Fig. 5.

In order to verify the accuracy of the proposed method, this paper proposes a skin-stiffener verticality detection method. This method is calculated based on discrete FE node information, and all the nodes of the stiffeners connected to the skin are taken as verification nodes.

For the stiffeners part, the stiffener plane is defined by three nodes of the element that contains a verification node, and the three nodes are expressed as A_1, A_2 and A_3. At the same time, the skin plane is defined by three nodes that are near the verification node, and the three nodes are expressed as B_1, B_2 and B_3. The normal vectors of the two planes are calculated respectively by Eq. (4) and Eq. (5), and the normal vectors of the two planes are calculated respectively by Eq. (6). Finally, the results of skin-stiffener verticality for the integrally stiffened shell θ are calculated by the plane vector of skin and plane vectors of stiffener. The schematic diagrams of the skin-stiffener verticality detection method are displayed in Fig. 6.

$$n_1 = A_1A_2 \times A_1A_3 \tag{4}$$

$$n_2 = B_1B_2 \times B_1B_3 \tag{5}$$

$$\theta = arc\cos(\frac{n_1 \cdot n_2}{||n_1|| \cdot ||n_2||}) \tag{6}$$

Free-form deformation (FFD) method is a typical manifestation of geometry deformation, primarily proposed by Sederberg and Parry [60] in 1986. FFD has so far been applied in various fields such as geometry sculpt, computer animation, and ship hydrodynamic design. From the mathematical point of view, the FFD method realizes the mapping of the object to be deformed from the initial space to the final space by moving the control points. However, effort is also needed to build the control points, and it requires experience to manipulate control points.

In order to better compare the accuracy and efficiency of the two methods, a simple model is deformed with FFD and proposed method respectively. It should be noted that most of the available FFD methods are used for shape optimization, and thus it cannot be directly used for the purpose of mesh deformation in this
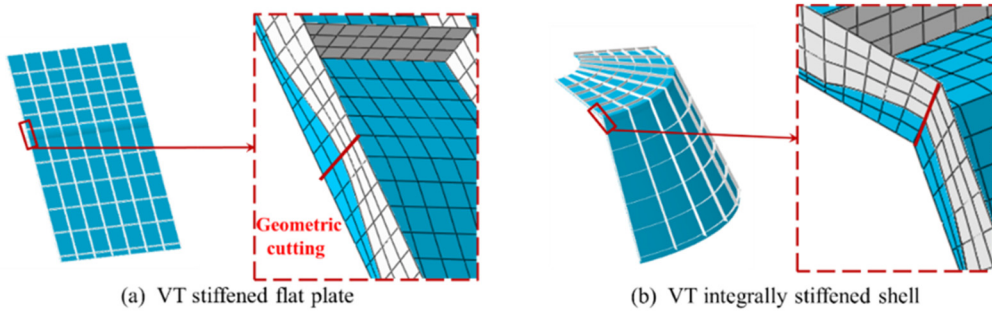
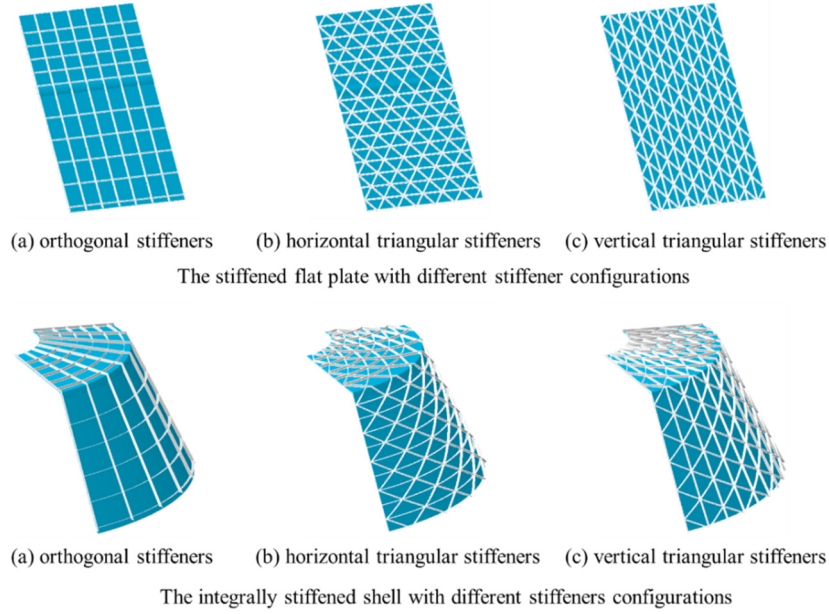**Fig. 4.** Schematic diagrams of the building VT integrally stiffened shell.

(a) orthogonal stiffeners (b) horizontal triangular stiffeners (c) vertical triangular stiffeners

The stiffened flat plate with different stiffener configurations

(a) orthogonal stiffeners (b) horizontal triangular stiffeners (c) vertical triangular stiffeners

The integrally stiffened shell with different stiffeners configurations

Fig. 5. Schematic diagrams of building stiffened flat plates and integrally stiffened shells with different stiffener configurations.

- Nodes of the stiffener element
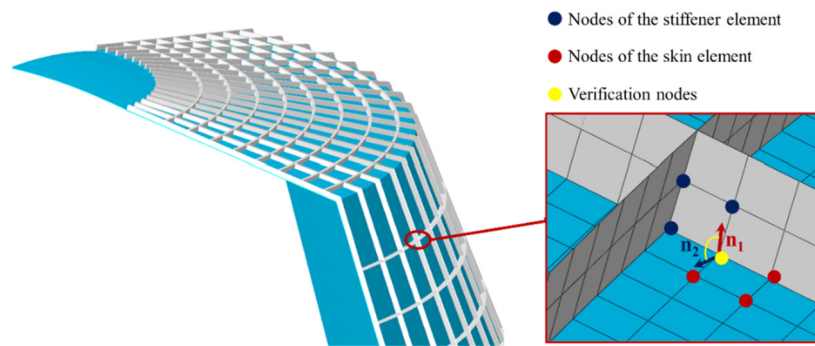- Nodes of the skin element
- Verification nodes

Fig. 6. Schematic diagram of the skin-stiffener verticality detection method.

manuscript. In this case, we propose a suitable method to implement FFD method in the mesh deformation framework, and the deformation process is shown in Fig. 7. For comparison, the identical control points with different numbers of 90, 924 and 15453 are used for FFD method and the proposed method respectively. Then, mesh deformations are carried out. The calculation time and average deviation angle after deformation with different control points are calculated, and detailed results are shown in Table 1. For example, when the number of control points is 90, the mean

deviation angle by the proposed method is 2.46°, which reduces by 20.6% than 3.10° by the FFD method, indicating the high modelling accuracy of the proposed method. In terms of computational efficiency, the modelling time by the proposed method is 0.30 s, which reduces by 41.2% than the modelling time of 0.51 s by the FFD method. And it can be found out through the comparison of results, the proposed method behaves better than FFD method in modelling accuracy and computational efficiency.
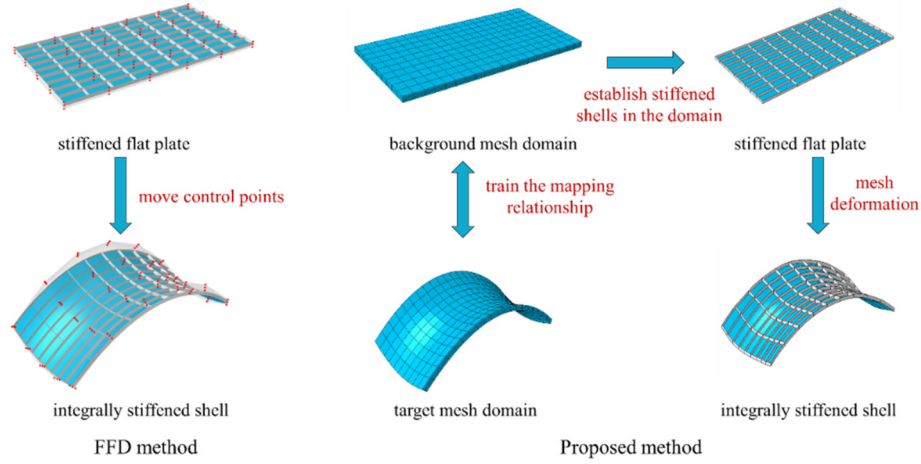
Fig. 7. Deformation diagram of FFD method and proposed method.

Table 1
Results comparison of FFD method and proposed method.

Number of control points	Method	Mean deviation angle (°)	Computing time (s)
90	FFD method	3.10	0.51
	Proposed method	2.46	0.30
924	FFD method	1.43	1.67
	Proposed method	1.28	0.67
15453	FFD method	1.05	50.06
	Proposed method	0.97	19.43

2.2. DNN method for layout optimization of the VT integrally stiffened shell

After the mesh deformation method is established, the layout optimization can be carried out for the VT integrally stiffened shell by the DNN method. The DNN optimization method is used to solve the optimization problem in this paper. DNN method is a novel machine learning method, which is widely used in object detection, image recognition, speech recognition and other fields. This section briefly introduces the basic principles of the DNN training based on Adaptive moments (Adam) algorithm. For a neural network with n hidden layers, its model parameters mainly include weight W and threshold b. The output of the jth layer of the DNN can be expressed as:

$$Z^{(j)} = f(W^{(j)}Z^{(j-1)} + b^{(j)}), \forall j \in 1, 2, \cdots, n \tag{7}$$

where $Z^{(j)}$ represents the output of the jth layer, $Z^{(j-1)}$ represents the output of the $(j-1)$th layer, and f represents the activation function. This article uses the ReLU [61] activation function.

W and b can be uniformly represented by the parameters $\theta = \{W^{(j)}, b^{(j)}\}$ $(j = 1, 2, \ldots, n + 1)$ and θ can be optimized by the minimum formula as:

$$L(\theta) = \frac{1}{N}\sum_{i=1}^{N} L_i = \frac{1}{N}\sum_{i=1}^{N}(y_i - f(x_i; \theta))^2 \tag{8}$$

where $L(\theta)$ represents the loss function of the model parameter θ, (x, y) is the training data, $f(x_i; \theta)$ is the DNN prediction result, N is the total number of sample points.

The iterative calculation format of Adam algorithm [62] is as follows:

$$\nabla L(\theta_l) = \frac{\partial L_{il}}{\partial \theta_l} \tag{9}$$

$$m_l = \beta_1 m_{l-1} + (1 - \beta_1)\nabla L(\theta_l) \tag{10}$$

$$v_l = \beta_2 v_{l-1} + (1 - \beta_2)[\nabla L(\theta_l)]^2 \tag{11}$$

where l represents the number of iteration steps, $\nabla L(\theta_l)$ represents the derivative of the loss function, m represents partial first-order moment estimation; v represents partial second-order moment estimation, β_1 and β_2 represent the attenuation of m and v.

Adam algorithm uses moving average to update model parameters:

$$\theta_{l+1} = \theta_l - \frac{\alpha m_l}{\sqrt{v_l + \varepsilon}} \tag{12}$$

where ε is a very small positive number to avoid division by zero, and α represents the learning rate.

The DNN optimization method mainly includes the following steps.

Step 1: According to the number of parameters and the complexity of the problem, the initial sampling points set is established firstly based on Latin Hypercube Sampling (LHS) method. The responses for the initial sampling points are calculated respectively.

Step 2: The DNN model is established with the initial sampling points. Then the weights and thresholds of the DNN model are trained based on the Adam algorithm.

Step 3: Genetic Algorithm (GA) optimization aiming at minimizing M is performed.

Step 4: The sampling points are updated by adding a new point found in step 3. The stop criterion is that the iteration number reaches the maximum value. Once the criterion is satisfied, the optimization is stopped. If the stop criterion is not satisfied, the new sampling point is added into the initial sample points set and the optimization is performed again. This process repeats until the stop criterion is satisfied.

In order to evaluate the prediction accuracy of the DNN model. The leave-one-out cross validation method is carried out in the design space. The R^2 value is used to evaluate the prediction accuracy of the DNN model.
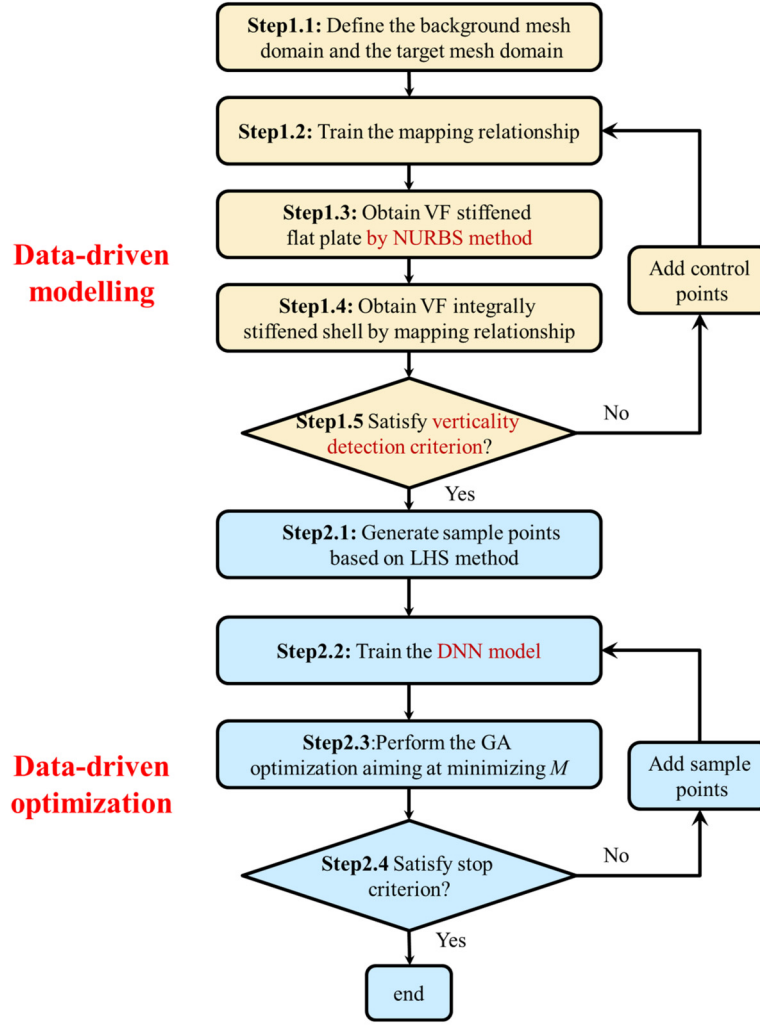
Fig. 8. Flow chart of data-driven modelling and optimization framework for the VT integrally stiffened shell.

$$R^2 = 1 - \frac{\sum_{i=1}^{k}(P_i - f(x_i))}{\sum_{i=1}^{k}(P_i - \overline{P_i})} \qquad (13)$$

where, k is the total number of sampling points of the surrogate model, P_i is the actual value of the ith sampling point of the surrogate model, $f(x_i)$ is the predicted value on x_i by the DNN model constructed using sampling points except x_i. $\overline{P_i}$ is the mean value of the actual values of all sampling points of the DNN model. The more R^2 approximates to 1.0, the more accurate the established DNN model is.

2.3. Data-driven modelling and optimization framework for the VT integrally stiffened shell

The VT mesh deformation modelling method based on RBF surrogate model and NURBS method is proposed in Section 2.1. The data-driven optimization framework based on the DNN method is established in Section 2.2. In conclusion, the data-driven modelling and optimization framework is established for the VT integrally stiffened shell in this section, as shown in Fig. 8. This section will introduce the flow chart of the data-driven modelling and optimization framework for the VT integrally stiffened shell in detail.

Firstly, the target mesh domain containing the design domain of the VT integrally stiffened shell and the background mesh domain that has similar topological features of the target mesh domain

are built in step 1.1. Then the RBF surrogate model is employed to train the mapping relationship between the coordinates of all nodes of the background mesh domain and the target mesh domain in step 1.2. Based on the NURBS method, the ET stiffened flat plate is transformed into VT stiffened flat plate in step 1.3 by moving the coordinates of nodes. Next, the VT stiffened flat plate is transformed into the VT integrally stiffened shell by the mapping relationship. Finally, the accuracy of the RBF surrogate model is verified by the skin-stiffener verticality detection method in step 1.5.

Since the VT integrally stiffened shell can be automatically modelled by mesh deformation, the DNN method is carried out for the VT integrally stiffened shell to search the optimal result. The initial sampling points based on LHS method is established in step 2.1. Based on above results, the DNN training model is established in step 2.2. Next, the GA optimization aiming at minimizing M is performed in step 2.3. If the optimization cannot satisfy the stop criterion, the new point is added to the sample points set and GA optimization is performed again in step 2.4. This process repeats until the stop criterion is satisfied. The detailed pseudo code introducing the steps of the modelling and optimization framework for the VT integrally stiffened shell is displayed in Algorithm 1.

Algorithm 1: Pseudo code of the modelling and optimization framework for the VT integrally stiffened shell.

1: The target mesh domain and the background mesh domain are defined containing the design domain
2: **While** the verticality detection criterion is not satisfied **do**
3:    The accuracy can be improved by sequential adding finite element nodes as new control points where θ is large
4:    The RBF surrogate model is employed to train the mapping relationship between these two control point sets
5:    The VT stiffened flat plate FE model is obtained by using NURBS method
6:    The VT stiffened flat plate is transformed into the VT integrally stiffened shell based on the mapping relationship
7:    The accuracy of the VT integrally stiffened shell is verified by the skin-stiffener verticality detection method
8: **End while**
9: The initial sampling points set is established based on LHS method
10: **While** the stop criterion is not satisfied **do**
11:    The DNN model is established with the sampling points
12:    GA optimization aiming at minimizing M is performed.
13:    The sampling points are updated by adding a new point
14: **End while**
15: Sort all the evaluated sample points by their responses to find X^{opt}
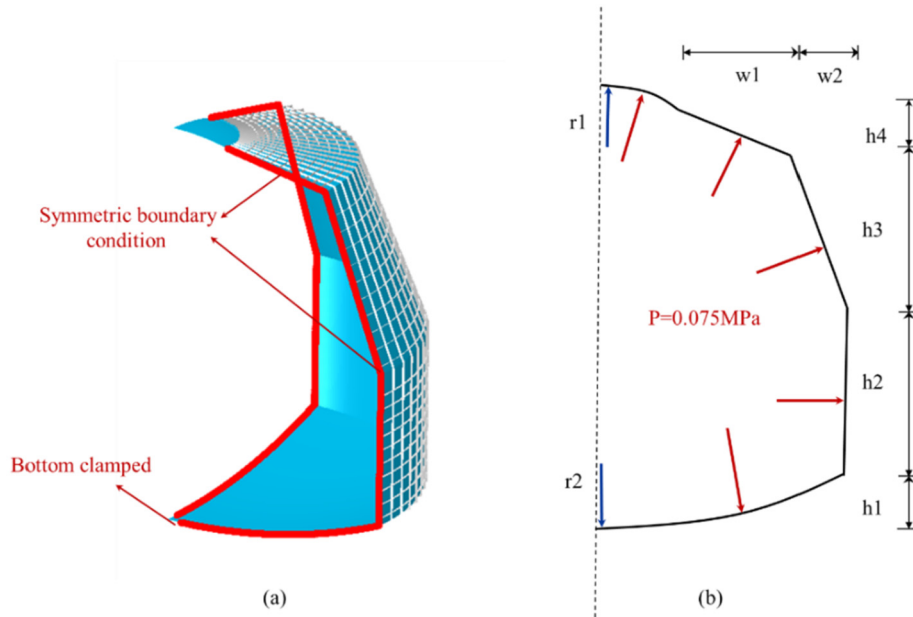
Fig. 9. Schematic diagrams of model dimensions, boundary condition and loading condition for the VT integrally stiffened shell. (a) 3D model; (b) axisymmetric 2D model.

3. Illustrative example of integrally stiffened shells

3.1. Model information for integrally stiffened shell under internal pressure

In order to verify the effectiveness of the proposed method, a representative example of the VT integrally stiffened shell under internal pressure is carried out, which is presented in Fig. 1 (b). The example of the VT integrally stiffened shell under internal pressure comes from the actual engineering designs, and their initial results refer to the details of the actual designs. It should be pointed out that the initial result represents the start point of the optimization process. As presented in Fig. 1 (c), a 1/4 model of the integrally stiffened shell is established. The skin is meshed by solid elements (C3D8R), and the shell is meshed by shell elements (S4R). Particularly, the element number along the stiffener height direction is 3 and the element number along the skin thickness direction is 2. ABAQUS is used for the FE analysis in this paper. The model is clamped at the bottom and symmetrical displacement boundary conditions are applied to both sides of the 1/4 model as the boundary condition. An internal pressure of P=0.05 MPa are imposed on the shell. Typical stainless-steel material properties are listed in Table 2.

Table 2
Material properties of integrally stiffened shell under internal pressure.

E (Gpa)	ν	ρ (t/mm³)
70	0.3	2.7E-9

The dimensions, boundary condition and loading condition of the VT integrally stiffened shell are shown in Fig. 9. The parameters $w1$ and $w2$ are 754.78 mm and 451.62 mm. The shell height $h1$, $h2$, $h3$, $h4$ of the VT integrally stiffened shell are 304.20 mm, 1017.58 mm, 1135.95 mm and 131.16 mm, respectively. The radii of the upper and lower spheres $r1$ and $r2$ are 1797.00 mm and 4460.30 mm. Dimensions of the VT integrally stiffened shell under internal pressure are listed in Table 3.

### 3.2. Data-driven modelling for integrally stiffened shell under internal pressure

By means of the mesh deformation method in Section 2.1, the FE models of the VT integrally stiffened shell can be established. As presented in Fig. 10, the optimization model consists of three parts: non-designable domain, VT skin and VT stiffeners. VT skin and VT stiffeners are obtained by the mesh deformation method.

Table 3
Dimensions of the VT integrally stiffened shell under internal pressure.

h1(mm)	h2(mm)	h3(mm)	h4(mm)	w1(mm)	w2(mm)	r1(mm)	r2(mm)
304.20	1017.58	1135.95	131.16	754.78	451.62	1797.00	4460.30
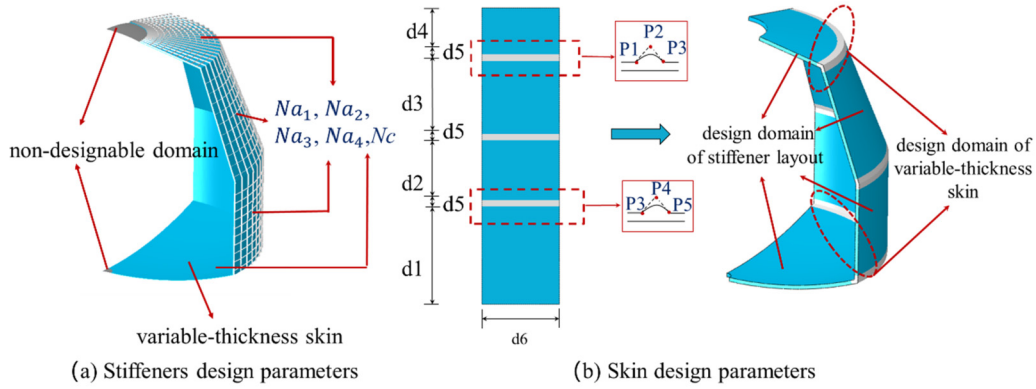
Fig. 10. Schematic diagrams of variables for stiffeners and skin.

Table 4
Dimensions of the flat plate.

| d1(mm)	d2(mm)	d3(mm)	d4(mm)	d5(mm)	d6(mm)
1508.78	917.58	1122.43	716.09	100.00	1000.00

Particularly, in order to improve the accuracy of training, the total number of control points for RBF surrogate model is 52256. 11882 points are picked as a set of angle inspection to verify the accuracy of the proposed method. By the method proposed in Section 2.1, the mapping relationship between the background mesh domain and the target mesh domain is trained by RBF surrogate model. Then the ET stiffened flat plate are established. Next the ET stiffened flat plate is transformed into the VT stiffened flat plate by the NURBS method. Based on the previously established high-precision RBF surrogate model, the VT stiffened flat plate is used to obtain the VT integrally stiffened shell by the mapping relationship. The schematic diagrams of variables for stiffeners and skin are displayed in Fig. 10. In this way, we can control the number and layout of the stiffeners of the flat plate, as well as the coordinates of the NURBS control points, to form the VT integrally stiffened shell. The dimensions of the flat plate are listed in Table 4. Finally, the VT integrally stiffened shell and the non-designable domain are assembled, then the loading condition and boundary condition are imposed on the FE model.

By the method of skin-stiffener verticality detection, average value of the detection results of skin-stiffener verticality for the integrally stiffened shell is 0.29°. As presented in Fig. 11, the number of element which angle greater than 89.5° and less than 90.5° is 11014, and the proportion of the total element is 92.27%.

After the RBF surrogate model is trained with high prediction accuracy, the modelling of the VT integrally stiffened shell is finished, and then the optimization based on the DNN method is carried out.

3.3. Optimization designs of VT integrally stiffened shell and ET integrally stiffened shell

In this section, the optimization for the VT integrally stiffened shell and the ET integrally stiffened shell are performed respectively. The optimization formulations of the VT integrally stiffened shell and the ET integrally stiffened shell are as follows,
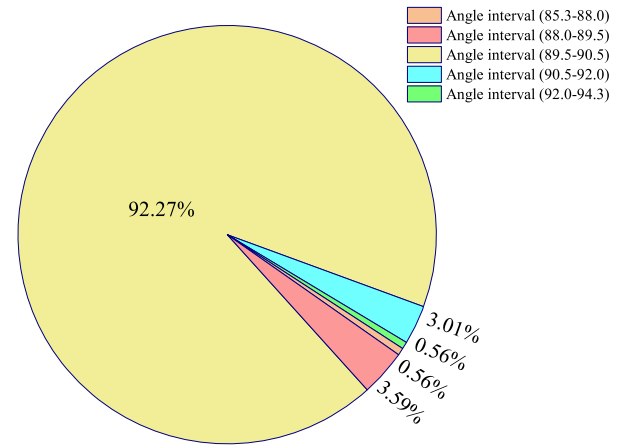
Fig. 11. Detection results of skin-stiffener verticality for the integrally stiffened shell under internal pressure.

$$Find : \mathbf{X} = [P_1, P_2, P_3, P_4, P_5, h_r, t_r, Na_1, Na_2, Na_3, Na_4, N_c]$$

$$Minimize : M$$

$$Subject\ to : U_{max} \leq U^0$$
$$S \leq S^0 \qquad\qquad (14)$$

where $\mathbf{X}$ is referred to as the design variables, including the height of 5 control points P_1, P_2, P_3, P_4 and P_5, the sum of skin thickness and stiffener height h_r, stiffener thickness t_r, axial number of stiffeners Na_j (j=1,2,3,4) and circumferential number of stiffeners N_c. M is the structural weight. U_{max} is the maximum displacement of the structure, and S is the ratio of elements that element stress exceeding 250 MPa to the total number of elements. Constraint conditions are set as follows: U^0 is 20.00 mm and S^0 is 0.59%, which are the initial results of U_{max} and S.
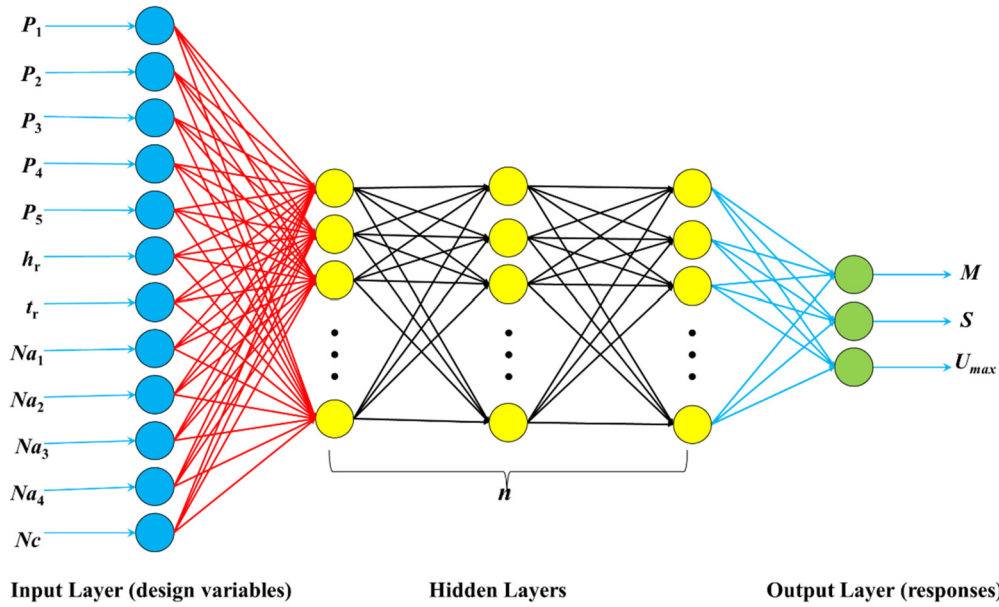
Fig. 12. Schematic diagrams of building DNN model.

Table 5
Prediction accuracy results of DNN models for the VT integrally stiffened shell under internal pressure.

R^2 of S	R^2 of U_{max}	R^2 of M
0.92	0.98	0.98

Table 6
Prediction accuracy results of DNN models for the ET integrally stiffened shell under internal pressure.

R^2 of S	R^2 of U_{max}	R^2 of M
0.98	0.98	0.99

As shown in Fig. 12, the DNN method is established based on the method proposed in Section 2.2. The details of the DNN model of the integrally stiffened shell are as follows: the number of hidden layers for U_{max}, M, S are 5, 8, 5, respectively; the number of neurons in each layer for U_{max}, M, S are 400, 800, 200, respectively. To evaluate the prediction accuracy of the DNN model, the leave-one-out cross validation method is carried out in the design space. The R^2 values of the DNN model are listed in Table 5 and Table 6. The iteration history of optimization for integrally stiffened shell under internal pressure are shown in Fig. 13.

The optimal result (188.71 kg) of the VT integrally stiffened shell under internal pressure decreases by 10.31% than the ET integrally stiffened shell under internal pressure decreases (210.40 kg) (Table 7). The maximum displacement is 18.98 mm and the ratio of elements that element stress exceeding 250 MPa to the total number of elements is 0.44%, which satisfies the constraints. The configurations diagrams, displacement distribution diagrams and stress distribution diagrams are displayed in Fig. 14 and Fig. 15. Compared with the initial design, the layout of the stiffeners with ET integrally stiffened shell and variable- thickness integrally stiffened shell is similar, indicating that the stiffeners play a key role in improving the stiffness. And the displacement distribution diagrams are also similar, as shown in Fig. 15. As shown in Fig. 14, the optimization result of VT integrally stiffened shell is very obvious in terms of thickness distribution. Compared with the optimization result of ET integrally stiffened shell, the optimization result of VT integrally stiffened shell is that the closer to the corner
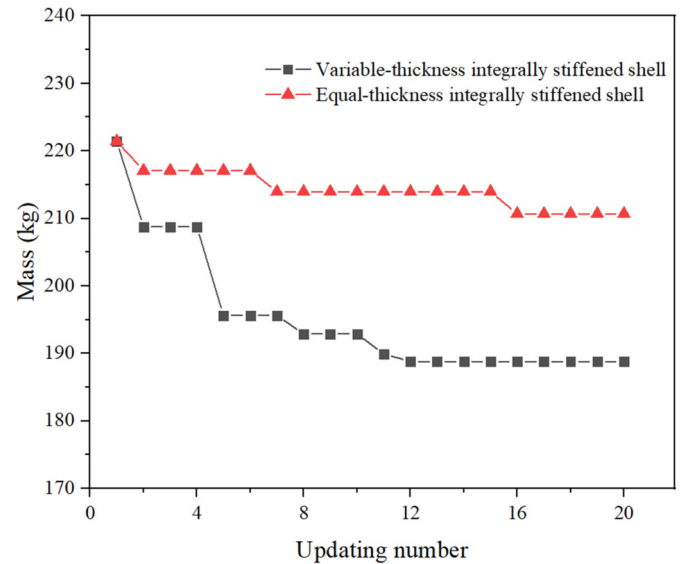

Fig. 13. Iteration history of optimization for integrally stiffened shell under internal pressure.

area, the greater the skin thickness. As shown in Fig. 15, the stress distribution diagrams of ET integrally stiffened shell and VT integrally stiffened shell show that both of them can improve the local strength, but the effect of VT integrally stiffened shell is better. It can be seen from the optimization results that some control points have reached the upper limit of the optimization design, and the weight of the VT integrally stiffened shell is lighter than that of the ET integrally stiffened shell. To sum up, the effectiveness of the proposed optimization framework is fully illustrated.
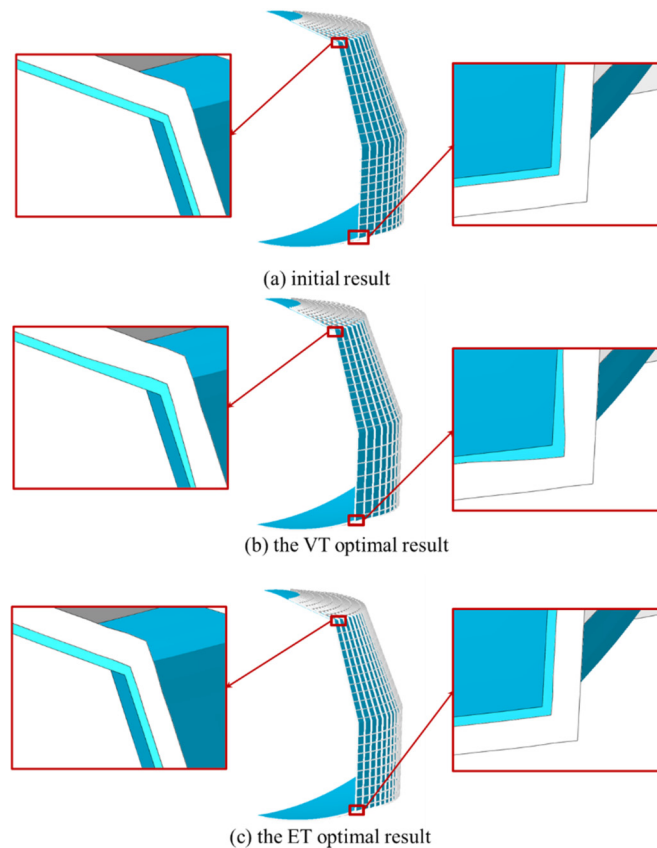
4. Conclusions

In this paper, a data-driven modelling and optimization framework is developed for the automatic design of the VT integrally stiffened shell, where the RBF surrogate model method and the NURBS method are used for FE modelling of the VT integrally stiffened shell and the DNN method is used for optimization of the

Table 7
Design space and optimal result of the VT integrally stiffened shell under internal pressure.

		Initial result	Lower bound	Upper bound	VT optimal result	ET optimal result
t_s (mm)	P_1	4.50	3.00	5.00	4.81	3.63
	P_2	4.50	3.00	10.00	5.88	3.63
	P_3	4.50	3.00	5.00	3.15	3.63
	P_4	4.50	3.00	10.00	8.75	3.63
	P_5	4.50	3.00	5.00	3.61	3.63
h_r (mm)		20.00	10.00	25.00	23.89	24.69
t_r (mm)		4.00	3.00	5.00	3.82	4.15
Na_1		10	5	15	7	10
Na_2		10	5	15	6	9
Na_3		10	5	15	13	11
Na_4		10	5	15	9	6
Nc		20	15	25	18	23
M (kg)		221.43	–	–	**188.71**	210.40
U_{max} (mm)		19.94	–	–	**18.98**	19.94
S (%)		0.59	–	–	**0.44**	0.41

(a) initial result

(b) the VT optimal result

(c) the ET optimal result

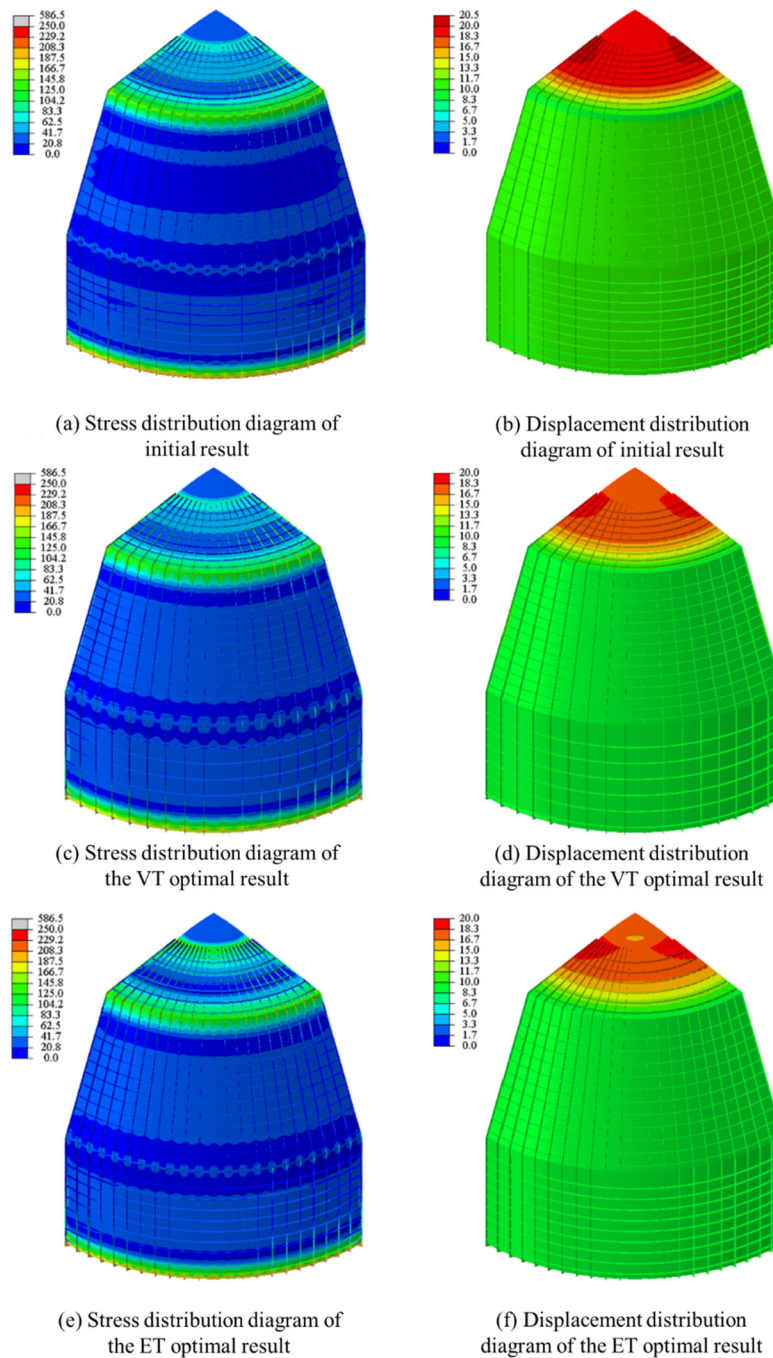**Fig. 14.** Configuration diagrams of the integrally stiffened shell under internal pressure.

VT integrally stiffened shell. In this way, the VT integrally stiffened shell can be obtained by modifying the layout of the stiffeners for the stiffened flat plate and the coordinates of the NURBS control points, which turn a modelling problem for complex surface into a modelling problem for flat plate. In order to verify the accuracy of the mesh deformation, a skin-stiffener verticality detection method is proposed in this paper. By the method of skin-stiffener verticality detection, average value of the detection results of skin-stiffener verticality for the integrally stiffened shell is 0.29°. The integrally stiffened shell under internal pressure as an example is presented to verify the effectiveness of the proposed data-driven modelling and optimization method. Optimizations for the VT integrally stiffened shell and the ET integrally stiffened shell are carried out. The

results show that, compared with the initial result and optimal result of the ET integrally stiffened shell, the optimal result of the VT integrally stiffened shell proposed in this paper achieves a structural weight reduction of 14.77% and 10.31%, respectively.

In future work, more advanced data-driven techniques will be studied to develop more efficient and effective modelling and optimization methods for the VT integrally stiffened shell.

Declaration of competing interest

The authors declare that they have no known competing financial interests or personal relationships that could have appeared to influence the work reported in this paper.

(a) Stress distribution diagram of initial result

(b) Displacement distribution diagram of initial result

(c) Stress distribution diagram of the VT optimal result

(d) Displacement distribution diagram of the VT optimal result

(e) Stress distribution diagram of the ET optimal result

(f) Displacement distribution diagram of the ET optimal result

Fig. 15. Stress and displacement distribution diagrams of the integrally stiffened shell under internal pressure.

Data availability statement

The data that support the findings of this study are available from the corresponding author, [KT], upon reasonable request.

Funding

References

[1] S.M.B. Afonso, J. Sienz, F. Belblidia, Structural optimization strategies for simple and integrally stiffened plates and shells, Eng. Comput. 22 (4) (2005) 429–452.

[2] O. Dababneh, T. Kipouros, Influence of high fidelity structural models on the predicted mass of aircraft wing using design optimization, Aerosp. Sci. Technol. 79 (2018) 164–173.

[3] A. Gomez, H. Smith, Liquid hydrogen fuel tanks for commercial aviation: structural sizing and stress analysis, Aerosp. Sci. Technol. 95 (2019) 105438.

[4] F. Morovat, A. Mozaffari, J. Roshanian, et al., A novel aspect of composite sandwich fairing structure optimization of a two-stage launch vehicle (Safir) using multidisciplinary design optimization independent subspace approach, Aerosp. Sci. Technol. 84 (2019) 865–879.

[5] W.C.H. Slemp, R.K. Bird, R.K. Kapania, et al., Design, optimization, and evaluation of integrally stiffened Al-7050 panel with curved stiffeners, J. Aircr. 48 (4) (2011) 1163–1175.

[6] G.D. Hopson, R.L. Grant, Pressurized modules for space station freedom, Space Technol. Ind. Commerc. Appl. 13 (3) (1993) 231–243.

[7] D. Boggiatto, A. Sferlazzo, The family of italian pressurized structures for the international space station scenario, Acta Astronaut. 44 (7–12) (1999) 553–560.

[8] Y.S. Lee, Y.W. Kim, Vibration analysis of rotating composite cylindrical shells with orthogonal stiffeners, Comput. Struct. 69 (2) (1998) 271–281.

[9] D. Van Dung, Analytical investigation on mechanical buckling of FGM truncated conical shells reinforced by orthogonal stiffeners based on FSDT, Compos. Struct. 159 (2017) 827–841.

[10] G.H. Rahimi, M. Zandi, S.F. Rasouli, Analysis of the effect of stiffener profile on buckling strength in composite isogrid stiffened shell under axial loading, Aerosp. Sci. Technol. 24 (1) (2013) 198–203.

[11] D. Wang, M.M. Abdalla, Global and local buckling analysis of grid-stiffened composite panels, Compos. Struct. 119 (2015) 767–776.

[12] N.D. Duc, S.E. Kim, D.T. Manh, et al., Effect of eccentrically oblique stiffeners and temperature on the nonlinear static and dynamic response of S-FGM cylindrical panels, Thin-Walled Struct. 146 (2020) 106438.

[13] T.Q. Quan, N.H. Cuong, N.D. Duc, Nonlinear buckling and post-buckling of eccentrically oblique stiffened sandwich functionally graded double curved shallow shells, Aerosp. Sci. Technol. 90 (2019) 169–180.

[14] B. Wang, K. Tian, C. Zhou, et al., Grid-pattern optimization framework of novel hierarchical stiffened shells allowing for imperfection sensitivity, Aerosp. Sci. Technol. 62 (2017) 114–121.

[15] B. Wang, P. Hao, G. Li, et al., Optimum design of hierarchical stiffened shells for low imperfection sensitivity, Acta Mech. Sin. 30 (3) (2014) 391–402.

[16] A. Semmani, Z. Sereir, Y. Hamou, Analysis and optimization of composite kagome grid panels subjected to the low velocity impact, J. Dyn. Behav. Mater. 6 (3) (2020) 287–302.

[17] C.L. Lai, J.B. Wang, C. Liu, Parameterized finite element modelling and buckling analysis of six typical composite grid cylindrical shells, Appl. Compos. Mater. 21 (5) (2014) 739–758.

[18] B. Wang, K. Tian, P. Hao, et al., Numerical-based smeared stiffener method for global buckling analysis of grid-stiffened composite cylindrical shells, Compos. Struct. 152 (2016) 807–815.

[19] H.J. Chen, S.W. Tsai, Analysis and optimum design of composite grid structures, J. Compos. Mater. 30 (4) (1996) 503–534.

[20] K. Tian, B. Wang, P. Hao, et al., A high-fidelity approximate model for determining lower-bound buckling loads for stiffened shells, Int. J. Solids Struct. 148 (2018) 14–23.

[21] K. Tian, B. Wang, K. Zhang, et al., Tailoring the optimal load-carrying efficiency of hierarchical stiffened shells by competitive sampling, Thin-Walled Struct. 133 (2018) 216–225.

[22] S. Jiang, F. Sun, H. Fan, Multi-failure theory of composite orthogrid sandwich cylinder, Aerosp. Sci. Technol. 70 (2017) 520–525.

[23] H.M.A. Abdalla, D. Casagrande, Analytical thickness distribution for minimum compliance axisymmetric vessels, Thin-Walled Struct. 149 (2020) 106641.

[24] R.C. Carbonari, P.A. Munoz-Rojas, E.Q. Andrade, et al., Design of pressure vessels using shape optimization: an integrated approach, Int. J. Press. Vessels Piping 88 (5–7) (2011) 198–212.

[25] K. Magnucki, J. Lewiński, Fully stressed head of a pressure vessel, Thin-Walled Struct. 38 (2) (2000) 167–178.

[26] W. Zhao, R.K. Kapania, Vibration analysis of curvilinearly stiffened composite panel subjected to in-plane loads, AIAA J. 55 (3) (2016) 981–997.

[27] R.R. Hiemstra, K.M Shepherd, M.J. Johnson, et al., Towards untrimmed NURBS: CAD embedded reparameterization of trimmed B-rep geometry using frame-field guided global parameterization, Comput. Methods Appl. Mech. Eng. 369 (2020) 113227.

[28] Y. Yang, S. Özgen, H. Kim, Improvement in the spring analogy mesh deformation method through the cell-center concept, Aerosp. Sci. Technol. 115 (2021) 106832.

[29] A.K. Michler, Aircraft control surface deflection using RBF-based mesh deformation, Int. J. Numer. Methods Eng. 88 (10) (2011) 986–1007.

[30] A.M. Morris, C.B. Allen, T.C.S. Rendall, CFD-based optimization of aerofoils using radial basis functions for domain element parameterization and mesh deformation, Int. J. Numer. Methods Fluids 58 (8) (2008) 827–860.

[31] S. Feng, W. Zhang, L. Meng, et al., Stiffener layout optimization of shell structures with B-spline parameterization method, Struct. Multidiscip. Optim. 63 (2021) 2637–2651.

[32] S. Porziani, C. Groth, W. Waldman, et al., Automatic shape optimisation of structural parts driven by BGM and RBF mesh morphing, Int. J. Mech. Sci. 189 (2021) 105976.

[33] J. Niu, J. Lei, J. He, Radial basis function mesh deformation based on dynamic control points, Aerosp. Sci. Technol. 64 (2017) 122–132.

[34] C.N. Li, Q. Wei, C.L. Gong, et al., An efficient multiple point selection study for mesh deformation using radial basis functions, Aerosp. Sci. Technol. 71 (2017) 580–591.

[35] K. Tian, H.Q. Li, L. Huang, et al., Data-driven modelling and optimization of stiffeners on undevelopable curved surfaces, Struct. Multidiscip. Optim. 62 (6) (2020) 3249–3269.

[36] B. Wang, K. Tian, H. Zhao, et al., Multilevel optimization framework for hierarchical stiffened shells accelerated by adaptive equivalent strategy, Appl. Compos. Mater. 24 (3) (2017) 575–592.

[37] B. Keshtegar, P. Hao, Y. Wang, et al., An adaptive response surface method and Gaussian global-best harmony search algorithm for optimization of aircraft stiffened panels, Appl. Soft Comput. 66 (2018) 196–207.

[38] K. Tian, J. Zhang, X. Ma, et al., Buckling surrogate-based optimization framework for hierarchical stiffened composite shells by enhanced variance reduction method, J. Reinf. Plast. Compos. 38 (21–22) (2019) 959–973.

[39] X. Yan, J. Zhu, M. Kuang, et al., Aerodynamic shape optimization using a novel optimizer based on machine learning techniques, Aerosp. Sci. Technol. 86 (2019) 826–835.

[40] Y. Song, X. Miao, L. Cheng, et al., The feasibility criterion of fuel-optimal planetary landing using neural networks, Aerosp. Sci. Technol. 116 (2021) 106860.

[41] L. He, N. Aouf, B. Song, Explainable deep reinforcement learning for UAV autonomous path planning, Aerosp. Sci. Technol. 118 (2021) 107052.

[42] R. Xie, A.G. Dempster, An on-line deep learning framework for low-thrust trajectory optimisation, Aerosp. Sci. Technol. 118 (2021) 107002.

[43] S.A. Renganathan, R. Maulik, J. Ahuja, Enhanced data efficiency using deep neural networks and Gaussian processes for aerodynamic design optimization, Aerosp. Sci. Technol. 111 (2021) 106522.

[44] X. Du, P. He, J.R.R.A. Martins, Rapid airfoil design optimization via neural networks-based parameterization and surrogate modeling, Aerosp. Sci. Technol. 113 (2021) 106701.

[45] Z.C. Li, K. Tian, H.Q. Li, et al., A competitive variable-fidelity surrogate-assisted CMA-ES algorithm using data mining techniques, Aerosp. Sci. Technol. 119 (2021) 107084.

[46] K. Tian, Z.C. Li, L. Huang, et al., Enhanced variable-fidelity surrogate-based optimization framework by Gaussian process regression and fuzzy clustering, Comput. Methods Appl. Mech. Eng. 366 (2020) 113045.

[47] K. Tian, Z. Li, J. Zhang, et al., Transfer-learning based variable-fidelity surrogate model for shell buckling prediction, Compos. Struct. 273 (2021) 114285.

[48] B. Miller, L. Ziemiański, Optimization of dynamic behavior of thin-walled laminated cylindrical shells by genetic algorithms and deep neural networks supported by modal shape identification, Adv. Eng. Softw. 147 (2020) 102830.

[49] A. Oishi, G. Yagawa, Computational mechanics enhanced by deep learning, Comput. Methods Appl. Mech. Eng. 327 (2017) 327–351.

[50] K.M. Hamdia, H. Ghasemi, Y. Bazi, et al., A novel deep learning-based method for the computational material design of flexoelectric nanostructures with topology optimization, Finite Elem. Anal. Des. 165 (2019) 21–30.

[51] M. Tovey, J. Owen, Sketching and direct CAD modelling in automotive design, Des. Stud. 21 (6) (2000) 569–588.

[52] J. Zhang, S. Chowdhury, A. Messac, An adaptive hybrid surrogate model, Struct. Multidiscip. Optim. 46 (2) (2012) 223–238.

[53] D.K.J. Lin, T.W. Simpson, W. Chen, Sampling strategies for computer experiments: design and analysis, Int. J. Reliab. Appl. 2 (3) (2001) 209–240.

[54] S. Ozcanan, A.O. Atahan, RBF surrogate model and EN1317 collision safety-based optimization of two guardrails, Struct. Multidiscip. Optim. 60 (1) (2019) 343–362.

[55] R. Jin, W. Chen, T.W. Simpson, Comparative studies of metamodelling techniques under multiple modelling criteria, Struct. Multidiscip. Optim. 23 (1) (2001) 1–13.

[56] B. Fornberg, E. Lehto, Stabilization of RBF-generated finite difference methods for convective PDEs, J. Comput. Phys. 230 (6) (2011) 2270–2285.

[57] C.K. Au, M.M.F. Yuen, Unified approach to NURBS curve shape modification, Comput. Aided Des. 27 (2) (1995) 85–93.

[58] W.J. Zhang, F. Zhang, G.H. Zhang, Research on a algorithm of adaptive interpolation for NURBS curve, Appl. Mech. Mater. 687 (2014) 1600–1603, Trans. Tech. Publications Ltd.

[59] L. Piegl, W. Tiller, The NURBS Book, Springer Science & Business Media, 1996.

[60] T.W. Sederberg, S.R. Parry, Free-form deformation of solid geometric models, in: Proceedings of the 13th Annual Conference on Computer Graphics and Interactive Techniques, 1986, pp. 151–160.

[61] M. Courbariaux, Y. Bengio, J.P. David, Binary connect: training deep neural networks with binary weights during propagations, Adv. Neural Inf. Process. Syst. (2015) 3123–3131.

[62] P. Devan, N. Khare, An efficient XGBoost–DNN-based classification model for network intrusion detection system, Neural Comput. Appl. 19 (2020) 1–16.